

See discussions, stats, and author profiles for this publication at: <https://www.researchgate.net/publication/263054162>

Effect of Oleic Acid Concentration on the Physicochemical Properties of Cobalt Ferrite Nanoparticles

ARTICLE in THE JOURNAL OF PHYSICAL CHEMISTRY C · JUNE 2014

Impact Factor: 4.77 · DOI: 10.1021/jp500578f

CITATIONS

5

READS

216

5 AUTHORS, INCLUDING:



Sonja Jovanović

Vinča Institute of Nuclear Sciences

3 PUBLICATIONS 12 CITATIONS

SEE PROFILE



Melita Tramšek

Jožef Stefan Institute

47 PUBLICATIONS 337 CITATIONS

SEE PROFILE



Zvonko Trontelj

University of Ljubljana

146 PUBLICATIONS 733 CITATIONS

SEE PROFILE



Danilo Suvorov

Jožef Stefan Institute

226 PUBLICATIONS 2,540 CITATIONS

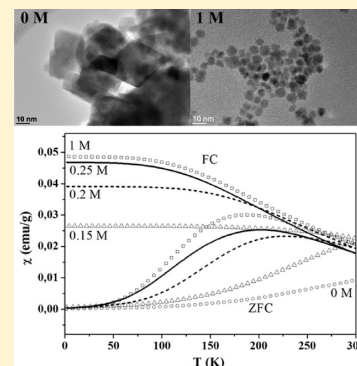
SEE PROFILE

Effect of Oleic Acid Concentration on the Physicochemical Properties of Cobalt Ferrite Nanoparticles

Sonja Jovanović,[†] Matjaž Spreitzer,^{*,†} Melita Tramšek,[‡] Zvonko Trontelj,[§] and Danilo Suvorov[†][†]Advanced Materials Department, Jožef Stefan Institute, Jamova 39, 1000 Ljubljana, Slovenia[‡]Department of Inorganic Chemistry and Technology, Jožef Stefan Institute, Jamova 39, 1000 Ljubljana, Slovenia[§]Institute of Mathematics, Physics and Mechanics, Jadranska ulica 19, 1000 Ljubljana, Slovenia

S Supporting Information

ABSTRACT: We have investigated the effect of oleic acid concentration on the physicochemical properties of solvothermally derived cobalt ferrite nanoparticles (CFO NPs). Without the oleic acid, agglomerated nanoplatelets with a crystallite size of about 19 nm were obtained, according to X-ray diffraction (XRD) and transmission electron microscopy (TEM). However, the addition of oleic acid decreases the size of the CFO NPs and at critical concentration, which was determined to be 0.25 M, well-dispersed, nonagglomerated spherical particles of about 6 nm were obtained. A further increase in the oleic acid concentration affected the particle size only slightly, with a relatively constant surface coverage of the oleic acid ligand. The results of our study indicate that particle-size control was achieved by bridging bidentate interactions between the oleic acid molecules and the metal atoms on the surface of the NPs, as determined by Fourier transform infrared spectra. These interactions affected the surface strain of NPs considerably, but kept the initial cation redistribution according to the Raman spectra. The room temperature magnetic measurements revealed that oleic acid enables us to effectively control the magnetic behavior of the CFO, which changes from ferrimagnetic to superparamagnetic at a critical concentration. Interparticle interactions are further interpreted by using low-temperature magnetic measurements, which also showed decreased surface anisotropy for samples prepared with oleic acid concentration above the critical value. An investigation of the treatment time showed that the capping with oleic acid is already achieved after 1 h of synthesis, but in order to improve the crystallization and consequently achieve the desired magnetic response a synthesis time of at least 4 h is required.



1. INTRODUCTION

Magnetic nanoparticles have recently attracted considerable attention due to their potential applications in optics,^{1,2} electronics,³ ferrofluids,^{4–6} biomedicine,^{7,8} recording media,^{9,10} etc. Among the various magnetic materials, cobalt ferrite (CoFe₂O₄, CFO) has often been investigated because of its high coercivity, moderate saturation magnetization, large magnetocrystalline anisotropy, large magnetostrictive coefficient, chemical stability, and mechanical hardness.^{11,12}

There are a number of methods used for the synthesis of CFO nanoparticles (NPs), like coprecipitation,¹³ the sol–gel reaction,¹⁴ the microemulsion method,^{15,16} the thermal decomposition method,¹⁷ the mechanochemical method,¹⁸ etc. However, coprecipitation has some advantages over the other methods because it is a fast and high-yield synthesis route. Nevertheless, when using this method it is very difficult to control the size, shape, and agglomeration of the synthesized nanoparticles and, consequently, their magnetic properties.^{19,20} Nanoparticles prepared by the mechanochemical method can be irregular in shape,²¹ while the micellar method does not always lead to the formation of highly crystalline nanoparticles, because of the low synthesis temperature.²² Some problems were solved by using the thermal decomposition method, forming nanoparticles with various sizes and shapes by the

decomposition of organic precursors and solvents.^{17,23} The drawbacks of this method are the toxic reagents and the potentially harmful byproducts, which are difficult to remove from the as-prepared nanoparticles.²⁰

Since the size, shape, and agglomeration of magnetic nanoparticles influence their applicability, good control over these features is essential. The solvothermal method allows the selection of various solvents and surface agents, because of which it is capable of meeting the strict requirements mentioned earlier. In addition, compared to other methods, the solvothermal synthesis is a simple method with a high rate of reaction and a low temperature of operation,²⁴ and was therefore selected in our study for the synthesis of the CFO NPs.

Oleic acid is commonly used for the preparation of hydrophobic nanoparticles.^{20,25,26} As a surfactant the oleic acid provides the steric stabilization of the nanoparticles against the van der Waals and magnetic attractive interactions and thereby prevents their agglomeration.²⁷ It limits the growth of the NPs and prevents the Ostwald ripening process taking place

Received: January 17, 2014

Revised: May 22, 2014

Published: June 5, 2014

since its surface layer acts as a barrier to mass transfer.^{28,29} As a result, the presence of oleic acid also influences the magnetic properties of the NPs by tuning the distance between the particles and consequently their interactions.¹⁷

Although used extensively in the past, information about the effect of the oleic acid concentration on the particle size, morphology, and agglomeration remains scarce. In Gong et al.³⁰ the effect of only one concentration of oleic acid (4 g in 100 mL) on the properties of Fe₃O₄ nanoparticles was examined. They found that oleic acid, present in the form of a bilayer, hinders the Ostwald ripening and favors the preparation of monodispersed magnetic nanospheres.³⁰ In the case of Co nanoparticles, irregularly shaped black precipitates were usually obtained for an oleic acid/cobalt ratio of 0.15. However, once the molar ratio of the oleic acid increased to 0.6, the capping agent formed a densely packed monolayer on the surface of the nanoparticles, which stabilized them against any agglomeration and furthermore prevented the Co from oxidizing in the air.³¹

Limaye et al.³² investigated oleic acid-capped CFO NPs prepared by the coprecipitation method, after which the samples were annealed at several temperatures. They observed that after coprecipitation the oleic acid is covalently bonded to the surface of the NPs, which are, as a result, under strain and thus exhibit a high coercivity (H_C). Thermal annealing increased the particle size and consequently the saturation magnetization (M_S). In contrast to this the H_C decreased with the increase of annealing temperature due to the removal of oleic acid.³² On the other hand, Repko et al.²⁰ investigated the influence of different organic solvents, as well as the influence of different ratios of water to organic solvent on the solvothermally synthesized CFO NPs, wherein the concentration of oleic acid was unaltered. They showed that the particles' properties depend on the amount and type of alcohol used. By using 1-pentanol as a solvent, monodispersed particles with a better Fe/Co ratio and phase purity were obtained compared to experiments in which ethanol was used as a solvent. This was explained by the lower polarity of the 1-pentanol compared to the ethanol and thus it better dissolves the oleic acid. The efficient control of the size, shape, and agglomeration of the nanoparticles achieved with oleic acid was proven in various synthesis methods. For example, iron oxide nanocrystals prepared by thermal decomposition exhibited a well-defined shape and size if the synthesis proceeded in the presence of oleic acid.^{33–35}

As can be inferred from a literature survey, the oleic acid plays an important role in the control of the size, shape, and agglomeration of the magnetic nanoparticles. In Limaye et al.³² the bonding nature of the oleic acid was determined to have a critical effect on the magnetic properties; however, the NPs were prepared by coprecipitation followed by a thermal treatment, which yielded highly agglomerated NPs. In Repko et al.²⁰ well-dispersed, solvothermally derived CFO NPs were obtained. Although the same method was used as in our case, the concentration-dependent bonding of the oleic acid was not investigated. Therefore, in the present work the effect of oleic acid on the various physicochemical properties of the CFO NPs was systematically examined. The results indicate the presence of a critical concentration at which significant changes to the properties occur. Therefore, control of the oleic acid concentration alone allows fine-tuning of the size, morphology, and magnetic properties of the CFO NPs, but so far this has not been determined.

2. EXPERIMENTAL SECTION

2.1. Chemicals. Cobalt(II) nitrate hexahydrate (Co(NO₃)₂·6H₂O, Alfa Aesar), iron(III) nitrate nonahydrate (Fe(NO₃)₃·9H₂O, Alfa Aesar), 1-pentanol (C₅H₁₂O, Alfa Aesar), oleic acid (C₁₈H₃₄O₂, Alfa Aesar), *n*-hexane (C₆H₁₄, Merck, ACS), and sodium hydroxide (NaOH, ApplChem) were used as purchased.

2.2. Synthesis of CFO NPs. The CFO NPs were synthesized solvothermally, according to the method described by Repko et al.²⁰ In a typical synthesis, 10 mmol of NaOH was dissolved in 2 mL of distilled water in an autoclave tube with a capacity of 50 mL. After that 10 mL of 1-pentanol was added with vigorous stirring, followed by the addition of 3.8 mL of oleic acid, which is used as a capping agent. A total of 2 mmol of iron nitrate and 1 mmol of cobalt nitrate were dissolved in 18 mL of distilled water and the aqueous solution was poured into the above solution and kept under vigorous stirring for 2 h, after which the autoclave was closed and placed into an oven at 180 °C for 16 h. Then, the system was cooled naturally to room temperature, after which the obtained particles were separated from the liquid phase with a permanent magnet and the liquid phase was discarded. The particles were washed three times by redispersing in *n*-hexane and precipitating with ethanol. After each precipitation the particles were separated from the liquid phase with a permanent magnet. Finally, they were redispersed in *n*-hexane, transferred to the watch glass, and left to dry in air overnight. Following the same procedure, samples without and with 0.1, 0.15, 0.2, 0.25, 0.5, and 2 M oleic acid were synthesized. Furthermore, the influence of the synthesis time was investigated (1–16 h), where the concentration of oleic acid (1 M) remained unchanged.

2.3. Characterization. The crystal structure of prepared CFO NPs was analyzed by using X-ray diffraction (XRD). The XRD patterns of the samples were recorded at room temperature in the 20° ≤ 2θ ≤ 80° range (2θ step = 0.02° with a counting time of 3 s per step) using a diffractometer (AXS D4 Endeavor, Bruker) with Cu Kα radiation (λ = 1.5406 Å). The average crystallite size d_{XRD} was calculated from the full width at the half-maximum of the (311) peak by using the Scherrer formula:³⁶

$$d_{\text{XRD}} = \frac{K\lambda}{\beta \cos \theta} \quad (1)$$

where K is a shape factor with a typical value of 0.9 and β is the full width at half of the maximum intensity, which was corrected by using the Warren correction $\beta = (\beta_{\text{exp}}^2 - \beta_{\text{std}}^2)^{1/2}$, where β_{std} is instrumental line broadening determined by using LaB₆ standard.^{17,37}

The morphology of the as-prepared samples was examined with a transmission electron microscope (TEM, JEM-2100, JEOL) operated at 200 kV. Prior to the TEM analysis the powders were first dispersed in *n*-hexane and subjected to an ultrasonic treatment for about 10 min. A few drops of the suspension was placed on a carbon-coated copper grid and left to dry in the air. Particle size distribution was calculated on about 600 nanoparticles in different parts of the grid. TEM images were analyzed with Digital Micrograph (DM) software where the contour of each particle was manually defined and the area of the particles was afterward determined by DM software. Assuming that the particles have spherical shape the diameter of each particle was calculated, together with its standard deviation.³⁸

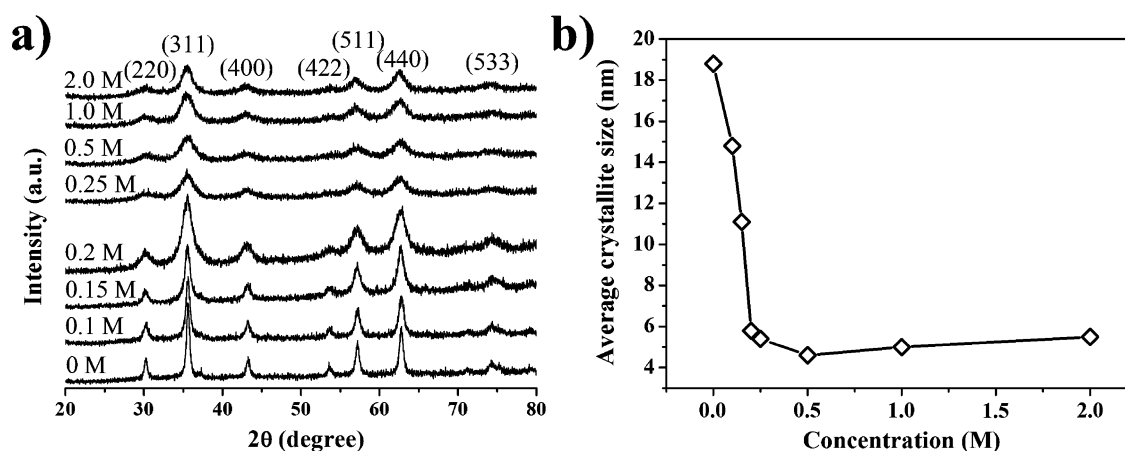


Figure 1. (a) XRD patterns of CFO NPs prepared with different concentrations of oleic acid. (b) The average crystallite size as a function of oleic acid concentration calculated by using the Scherrer formula.

Thermogravimetric (TG) analysis and differential scanning calorimetry (DSC) were performed on a Netzsch Jupiter 449 simultaneous thermal analysis (STA) instrument coupled with a Netzsch 403 C Aeolos quadrupole mass spectrometer (QMS). The curves were recorded in an argon/air (80/20) atmosphere from 25 to 900 °C with a heating rate of 10 °C/min, using a TG/DSC sample holder. TG measurement error is 2% of the measured value. Fourier transform infrared spectra (FT-IR) were recorded with an FTIR spectrometer Spectrum GX, PerkinElmer equipped with a MTEC Model 300 photoacoustic detector. The Raman spectra were recorded at room temperature with a Horiba Jobin Yvon LabRam-HR spectrometer equipped with an Olympus BXFM-ILHS Microscope and CCD detector. The samples were excited by the 632.8 nm emission line of a He–Ne laser with approximately 1.3 mW of power focused on a 1-μm spot on the surface of the sample through a 50× microscope objective. A vibrating-sample magnetometer (VSM, 7397 Lake Shore) was used to investigate the magnetic properties of the samples at room temperature in a maximum magnetic field of ± 15 kOe. VSM measurement error is 1% of the measured value. Low-temperature measurements (2–300 K) of the DC susceptibility (Zero Field Cooled-ZFC, Field Cooled-FC) in the 100 Oe magnetic field and magnetization (M) as a function of magnetic field (H) up to ± 50 kOe at $T = 5$ K were performed with a Quantum Design MPMS XL-5 (SQUID) magnetometer. The powder samples were fixed with wax in the sample holder to keep them mechanically stable during measurements. The temperature stability during magnetic measurement was within several mK at low temperatures and within 0.1 K at high temperatures. The relative error in all static magnetic measurements was less than 0.1%.

3. RESULTS AND DISCUSSION

3.1. XRD and TEM Analysis. Figure 1a shows the XRD patterns of the CFO NPs prepared with different concentrations of oleic acid. All the diffraction maxima correspond to the cubic spinel structure of CFO (JCPDS card no. 22–1086). As the oleic acid concentration increases to 0.25 M all the observed diffraction maxima become weaker and broader, while for higher concentrations similar patterns were obtained. These results indicate that up to 0.25 M the average crystallite size decreases with the oleic acid concentration, while further

addition of oleic acid has only a small influence on the average crystallite size (Figure 1b).

TEM images of the CFO NPs synthesized with different concentrations of oleic acid are shown in Figure 2. The results support the XRD findings and clearly show the same trend of particle size variation. A comparison of the average crystallite size from the XRD experiments with the particle size from the TEM analysis points to slightly larger values in the latter case. Particle size distribution for the samples prepared with 0.25–2 M oleic acid is shown in Figure S1 (see the Supporting

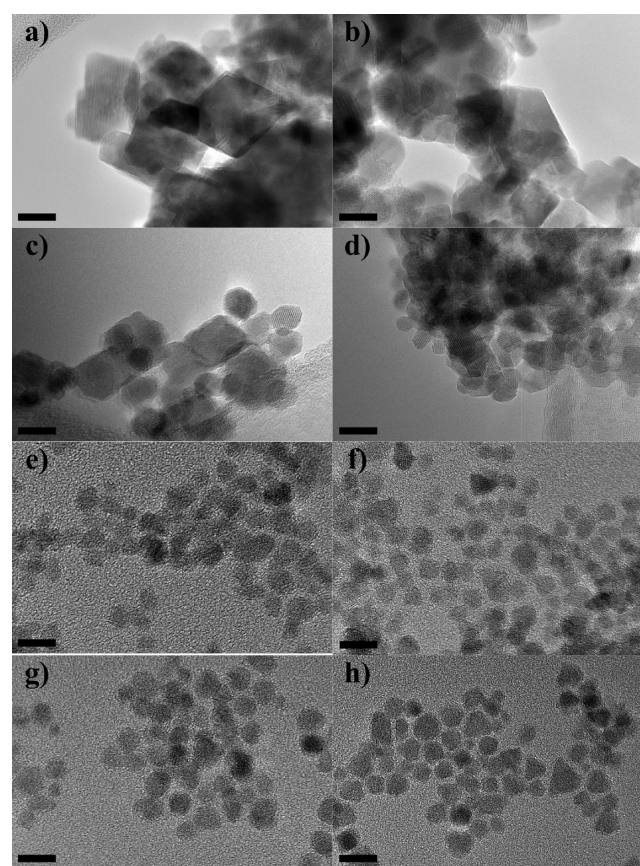


Figure 2. TEM images of CFO NPs synthesized with (a) 0, (b) 0.1, (c) 0.15, (d) 0.2, (e) 0.25, (f) 0.5, (g) 1, and (h) 2 M oleic acid. Scale bar is 10 nm.

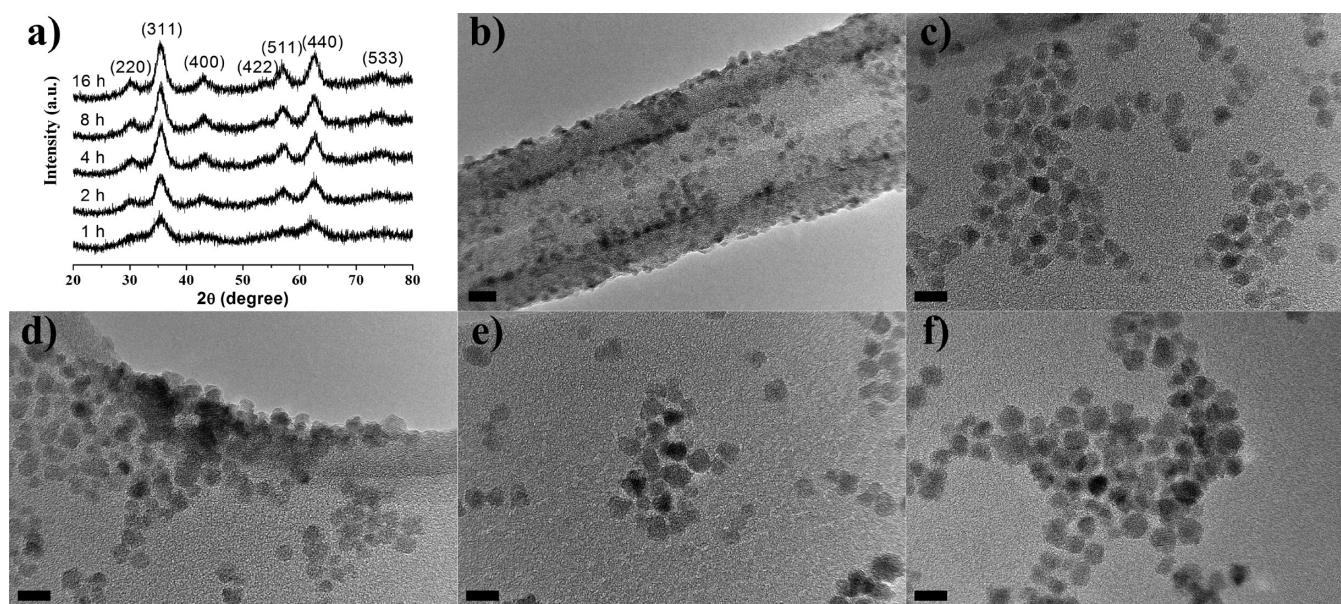


Figure 3. (a) XRD patterns and TEM images of CFO NPs with 1 M oleic acid synthesized at $T = 180\text{ }^{\circ}\text{C}$ for (b) 1, (c) 2, (d) 4, (e) 8, and (f) 16 h. Scale bar is 10 nm.

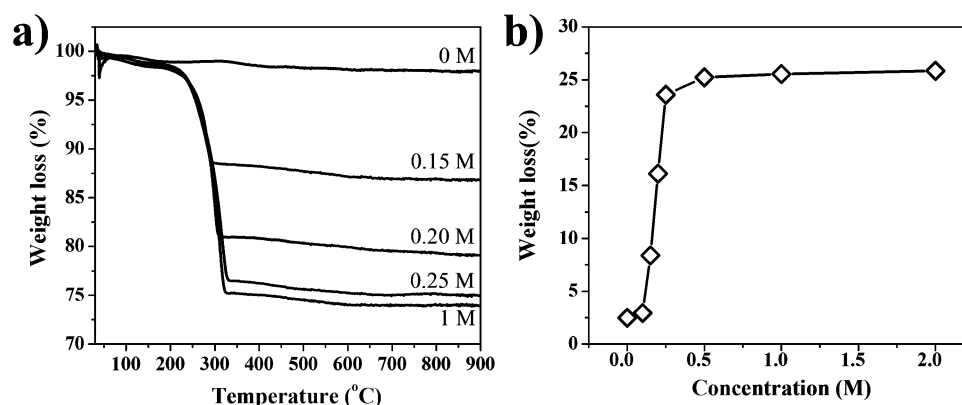


Figure 4. (a) TG plots of CFO NPs prepared with different concentrations of oleic acid. (b) Weight loss as a function of oleic acid concentration.

Information). The measured averaged diameter of CFO NPs prepared with 0.25, 0.5, 1, and 2 M is 5.9 ± 1.4 , 6.1 ± 1.2 , 5.9 ± 1.2 , and 6.9 ± 1.6 nm, respectively. However, the particle size distribution of 0–0.2 M samples was difficult to estimate due to particle agglomeration. Furthermore, the TEM analysis reveals that oleic acid also affects the particle morphology and agglomeration. Samples prepared without and with 0.1 M oleic acid (Figure 2a,b) consist of nanoplatelets (typical for CFO with an increased particle size), while the sample prepared with 0.15 M oleic acid (Figure 2c) consists of mixed sphere-like NPs and nanoplatelets that are smaller in size. A further increase in the oleic acid concentration showed the most pronounced change in the particle size and morphology and enabled the formation of sphere-like nanoparticles only, which are well dispersed (Figure 2d–h).

We further investigated the evolution of the NPs' size and morphology for samples solvothermally treated for 1, 2, 4, 8, and 16 h, with a constant concentration of oleic acid ($C_{\text{OA}} = 1$ M). The XRD patterns (Figure 3a) confirm the formation of single-phase CFO. The average crystallite size of the CFO NPs was almost independent of the synthesis time and was between 4 (1 and 2 h) and 5 nm (4, 8, and 16 h). Panels b–f of Figure 3 show TEM images of well-dispersed, sphere-like CFO NPs,

which are in the range 4–6 nm. Particle size distribution is shown in Figure S2 (see the Supporting Information) and the averaged diameter of NPs is 3.8 ± 0.7 (1 h), 4.8 ± 0.8 (2 h), 5.0 ± 0.9 (4 h), 5.3 ± 1.2 (8 h), and 5.9 ± 1.2 nm (16 h). Inhibition of the CFO NPs' growth can be explained by the oleic acid capping, which in the present experiment effectively served as a barrier to mass transfer.²⁹

The XRD and TEM analyses proved the crucial effect of the oleic acid on the NPs' stabilization, so in the continuation of this study the bonding characteristics of the oleic acid to the surface of the CFO NPs were examined in more detail.

3.2. TGA and FTIR Analysis. To determine the amount of adsorbed oleic acid and to identify the nature of its bonding to the surface, TG and FTIR analyses were performed. TG plots of samples prepared with different concentrations of oleic acid (C_{OA}) are presented in Figure 4a. In all cases, a slight weight loss (1–2%) was observed up to 180 °C due to the moisture content in the samples. A significant weight loss was observed at temperatures higher than 200 °C, especially for the samples prepared with $C_{\text{OA}} > 0.15$ M (Figure 4b). Up to 0.25 M the weight loss increases with oleic acid concentration and correlates to the numbers of oleic acid ligands attached to the surface of the CFO NPs. Above 0.25 M the weight loss

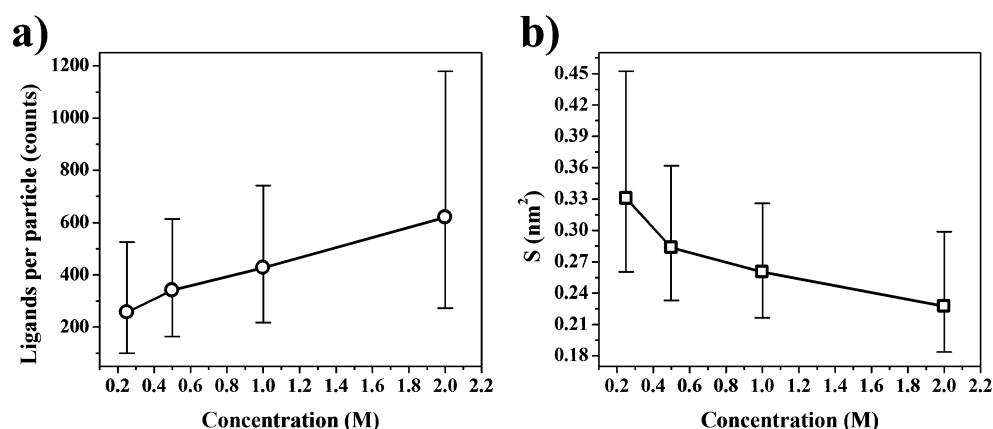


Figure 5. (a) Number of oleic acid ligands per particle and (b) their occupied surface area as a function of oleic acid concentration. The limits of N and S values were obtained by taking into account standard deviation of particle size distribution.

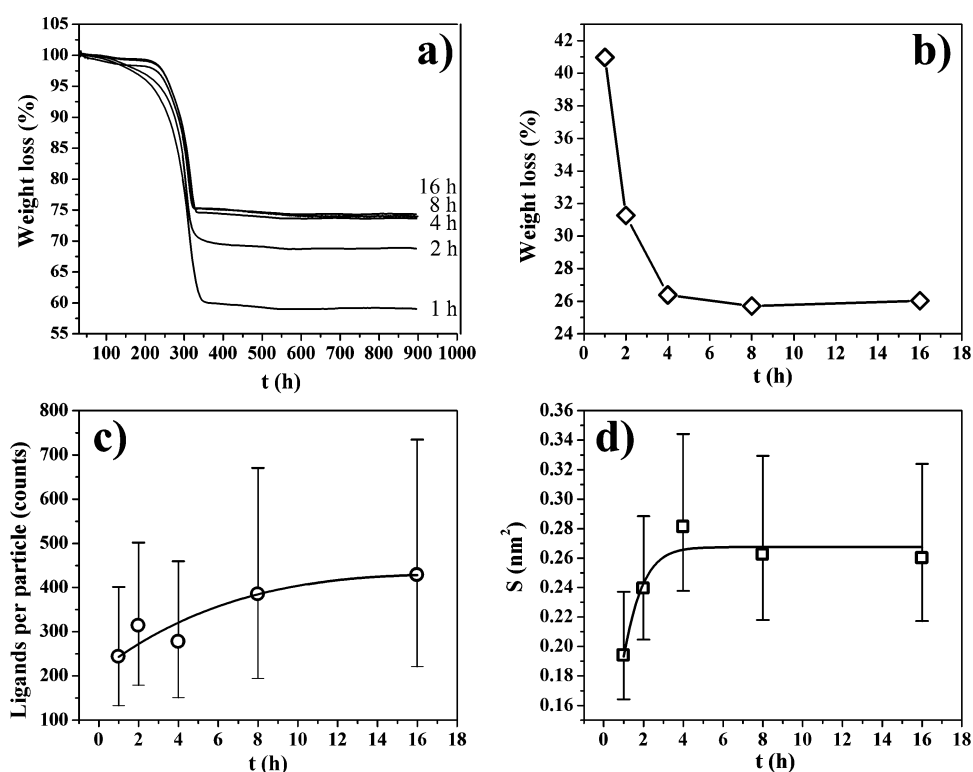


Figure 6. (a) TG plots of CFO NPs prepared with 1 M oleic acid for different synthesis times. (b) Weight loss as a function of synthesis time. (c) Number of oleic acid ligands per particle and (d) their surface area as a function of synthesis time. The limits of N and S values were obtained by taking into account standard deviation of particle size distribution.

saturates at 25%, which indicates the formation of a complete monolayer on the surface of the NPs.³⁹

The DSC curves of samples prepared with 0, 0.15, 0.2, 0.25, and 1 M oleic acid provide a detailed insight in the process of oleic acid removal and are presented in Figure S3 in the Supporting Information, together with TG results from Figure 4a. In the case of bare CFO NPs no marked endo- and/or exothermal process occurred (Figure S3, Supporting Information), which is further proved by the absence of corresponding QMS signals (Figure S4, Supporting Information). The DSC curves of oleic acid-coated samples show a distinct, single exothermal peak at about 300 °C related to oleic acid decomposition. Figure S4 in the Supporting Information shows that QMS spectra of different desorbing species match

DSC peak positions, while their intensity is proportional to the amount of oleic acid.

The measured weight loss was used to calculate the number of adsorbed oleic acid molecules per particle using the following equation:³²

$$N = \frac{4\rho r^3 \pi \omega N_A}{3(100 - \omega)M_{OA}} \quad (2)$$

where N is the number of oleic acid ligands per particle, $\rho = 5.3$ g/cm³ is the density of the CFO NPs, r is the average radius of the NPs (based on the TEM results, Figure 2), ω is the weight loss (in %), $N_A = 6.022 \times 10^{23}$ L/mol is Avogadro's constant, and $M_{OA} = 282.47$ g/mol is the molecular weight of oleic acid. The density of the CFO NPs was calculated by using the

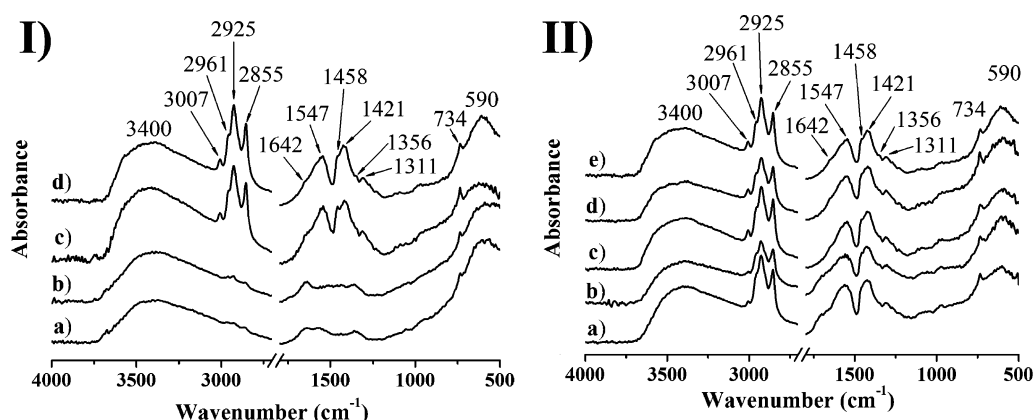


Figure 7. (I) FT-IR spectra of CFO NPs obtained solvothermally after a 16 h treatment. The CFO NPs were prepared (a) without and with (b) 0.15, (c) 0.25, and (d) 1 M oleic acid. (II) FT-IR spectra of CFO NPs solvothermally treated for (a) 1, (b) 2, (c) 4, (d) 8, and (e) 16 h in the presence of 1 M oleic acid.

formula $\rho = (8M_{\text{CFO}})/(N_A a^3)$, where $M_{\text{CFO}} = 234.62$ g/mol is the molecular weight of the CFO and $a = 8.38$ Å is its lattice constant.^{40,41} The number of ligands was calculated for samples prepared with 0.25–2 M oleic acid (Figure 5a), because only for these samples can the size of the NPs be unambiguously estimated from the TEM images (Figure 2e–h).

Assuming that the surface of the NPs is covered with a close-packed monolayer of the surfactant, the surface area S occupied by the oleic acid ligand indicates the ratio of the total surface area of the particles to the number of oleic acid ligands and can be calculated by using the following equation:⁴²

$$S = \frac{3(100 - \omega)M_{\text{OA}}}{N_A \rho \omega} \quad (3)$$

The calculated surface areas of the oleic acid ligands are presented in Figure 5b and are in good agreement with the reported values of 0.24,⁴² 0.28,⁴³ and 0.30 nm²,⁴⁴ for particles of nearly 10 nm. As the weight loss saturates for the samples with an oleic acid concentration between 0.5 and 2 M, the same coverage for a single oleic acid molecule is expected. The obtained results are in relatively good agreement with this expectation, taking into account the experimental error related to the determination of the particle size. However, the number of ligands per particle gradually increases with the oleic acid concentration and directly relates to the particle size increase, as determined with the TEM (Figure 2). The performed calculations confirmed that on the surface of the NPs the coverage of adsorbed surfactant molecules becomes larger with the concentration, but only up to a critical concentration, at which point the formation of the surfactant monolayer is complete.

Figure 4b shows that the amount of oleic acid on a particle's surface depends on its initial concentration. However, the measured weight loss was determined after a prolonged solvothermal treatment and, therefore, we examined the amount of adsorbed oleic acid as a function of the synthesis time. Figure 6a shows TG plots of samples synthesized for different synthesis times. As with the first set of samples, the initial weight loss up to 180 °C is due to a small amount of moisture present in the samples while at temperatures higher than 200 °C a significant weight loss was observed for all the samples and it decreased rapidly from 42% to 25% as the synthesis time increased (Figure 6b). DSC curves show a single exothermal peak related to oleic acid decomposition at about

300 °C (Figure S5, Supporting Information). The peak corresponds to QMS signals for desorbing fragments, while their intensity follows the trend of N and S (Figure S6, Supporting Information). It can be seen that the particle size simultaneously increases with the increase of the synthesis time. By taking this into account the number of oleic acid ligands per particle and the parameter S can be calculated (Figure 6c,d). Since the value of parameter S is relatively constant we can conclude that the stable oleic acid coverage was achieved after 4 h of solvothermal treatment. Thus, the drop in the amount of oleic acid with treatment time is due to the particles' different surface-to-volume ratio caused by the increase of their size. Namely, the weight loss depends on particle size in a similar way as surface-to-volume ratio. Furthermore, these results show that despite the complete coverage of the NPs with the surfactant, a slow growth occurs with the synthesis time.

To investigate the nature of the bonding of the oleic acid to the surface of the CFO NPs a FTIR analysis was performed. Figure 7, panel I, presents the FTIR spectra of the uncoated and oleic acid-coated CFO NPs. All the samples have a broad peak at 3400 cm⁻¹, which corresponds to the stretching vibrations of the hydroxide groups due to the moisture present in the samples.⁴⁵ The weak peak at 3007 cm⁻¹ is attributed to the C–H stretching of the =C–H group and it is present in the samples with 0.25 and 1 M oleic acid, while it is absent in the samples prepared without and with 0.15 M oleic acid. The weak shoulder at 2961 cm⁻¹ can be assigned to the asymmetric stretching of a –CH₃ group. The vibrations at 2925 and 2855 cm⁻¹ are attributed to the asymmetric and symmetric stretching of a –CH₂– group, respectively. These bands are more intense for samples with 0.25 and 1 M oleic acid than for the samples without and with 0.15 M oleic acid. The band at 1642 cm⁻¹ corresponds to the H–O–H scissoring from free or adsorbed water.^{25,46} This band appears as a shoulder in the samples with 0.25 and 1 M oleic acid and as a weak peak in the samples without and with 0.15 M oleic acid. Two new intense peaks at 1547 and 1421 cm⁻¹ are typical for the asymmetric and symmetric stretching of a COO⁻ group, respectively.²⁵ They were observed in the samples with 0.25 and 1 M oleic acid, but not in the samples without and with 0.15 M oleic acid. The bands observed as shoulders or weak peaks at 1458, 1356, and 1311 cm⁻¹ correspond to the –CH₂– scissoring, in-plane O–H bending, and C–O stretching, respectively.^{25,47} The band at ~734 cm⁻¹ belongs to the –CH₂– rocking vibration and the

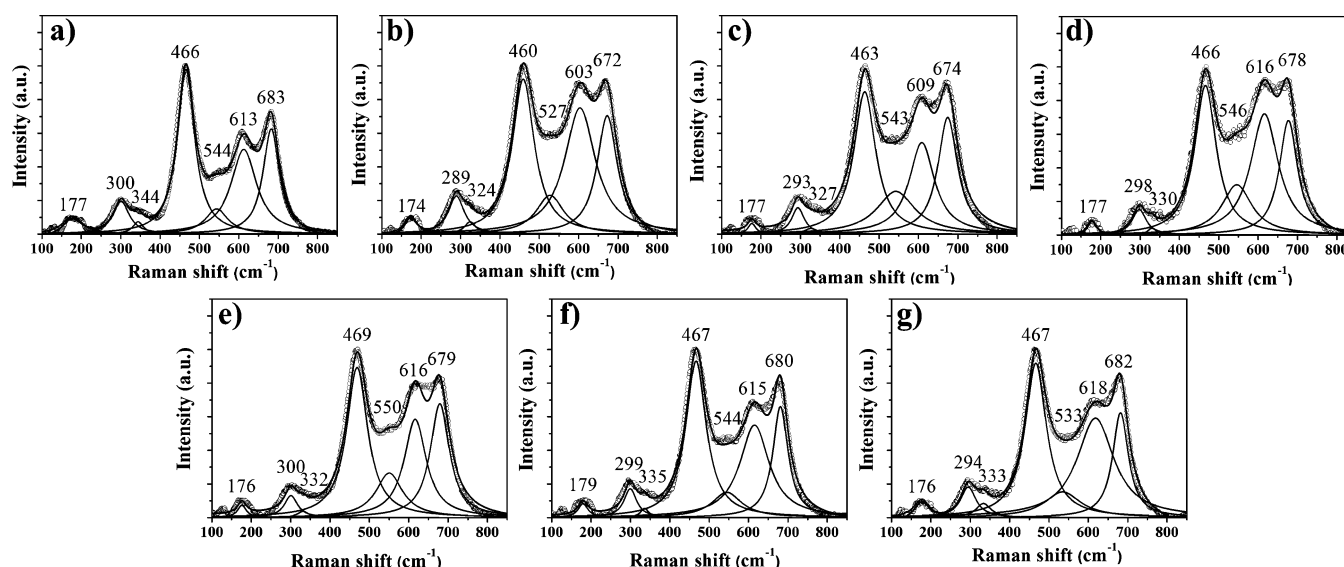


Figure 8. Raman spectra of samples prepared (a) without oleic acid and with (b) 0.1, (c) 0.15, (d) 0.2, (e) 0.25, (f) 1, and (g) 2 M oleic acid.

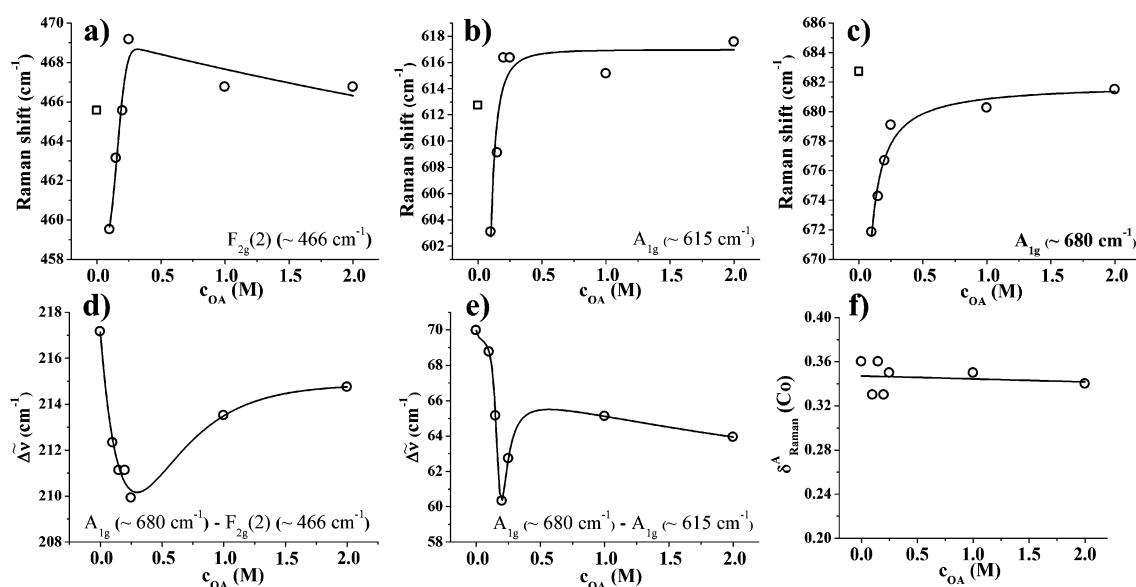


Figure 9. Raman shift of (a) $F_{2g}(2)$ ($\sim 466\text{ cm}^{-1}$), (b) A_{1g} ($\sim 615\text{ cm}^{-1}$), and (c) A_{1g} ($\sim 680\text{ cm}^{-1}$) modes as a function of oleic acid concentration. The sample prepared without oleic acid is indicated by the open square. The difference in the positions of (d) A_{1g} ($\sim 680\text{ cm}^{-1}$) - $F_{2g}(2)$ ($\sim 466\text{ cm}^{-1}$) and (e) A_{1g} ($\sim 680\text{ cm}^{-1}$) - A_{1g} ($\sim 615\text{ cm}^{-1}$) and (f) Co-content in tetrahedral site as a function of oleic acid concentration.

appearance of this band indicates that there are at least four methylenes in the row.⁴⁸ The intense peak at $\sim 590\text{ cm}^{-1}$ in all the samples is attributed to the stretching of the metal ion at the tetrahedral A-site, $M_A \leftrightarrow O$.^{32,49}

We assume that the amount of oleic acid in the sample with 0.15 M is small and thus below the detection limit of the FT-IR spectrometer. However, the intensity of the oleic acid vibration modes for the samples with 0.25 and 1 M is already strong enough to enable a determination of its bonding nature. In general, the type of interaction between the carboxylate head and the metal atom in the samples with 0.25 and 1 M oleic acid is indicated by the wavenumber separation, Δ , between the asymmetric and symmetric $-\text{COO}^-$ stretching. This interaction can be classified into four groups: monodentate, bridging bidentate, chelating bidentate, and ionic interaction. The largest Δ ($200\text{--}300\text{ cm}^{-1}$) corresponds to the monodentate interaction, the medium Δ ($110\text{--}200\text{ cm}^{-1}$) corresponds to

the bridging bidentate, and the smallest Δ ($<110\text{ cm}^{-1}$) corresponds to the chelating bidentate.^{25,32} In our work, Δ totals 126 cm^{-1} and corresponds to the bridging bidentate interactions, which indicate covalently bonded $-\text{COO}^-$ groups to the surface metal (Co and Fe) atoms.³²

In the present study, we also performed FT-IR analysis of samples prepared for different times (Figure 7, panel II). The results show that just after 1 h of synthesis the oleic acid is covalently bonded to the surface of NPs. This justifies TEM observation of small, well-dispersed CFO NPs (Figure 3b) and calculated values of parameter S (Figure 6d) which indicates a formation of complete monolayer. Also, based on the similarity of spectra (Figure 7, panel II), it can be concluded that the bonding nature of oleic acid and CFO is not influenced by synthesis time.

3.3. Raman Studies. CFO has an inverse spinel structure and in the ideal case all the divalent (Co^{2+}) cations occupy the

octahedral (B) sites, while the trivalent (Fe^{3+}) cations are equally divided between the octahedral (B) sites and the tetrahedral (A) sites.²⁸ In some cases the cations redistribute as $(\text{Co}_{\delta}^{2+}\text{Fe}_{1-\delta}^{3+})_{\text{A}}$ and $(\text{Co}_{1-\delta}^{2+}\text{Fe}_{1+\delta}^{3+})_{\text{B}}$, where δ is the cation distribution factor, which illustrates the fraction of tetrahedral (A) sites occupied by Co^{2+} cations.^{3,28} Cobalt ferrite has a cubic structure and belongs to the space group $Fd\bar{3}m$, where one complete unit cell contains 56 atoms ($Z = 8$).⁵⁰ A factor-group analysis predicts the following modes for the spinels:

$$\Gamma = \text{A}_{1g}(\text{R}) + \text{E}_g(\text{R}) + \text{F}_{1g} + 3\text{F}_{2g}(\text{R}) + \text{A}_{2u} + 2\text{E}_u + 4\text{F}_{1u}(\text{IR}) + 2\text{F}_{2u}$$

where the 4F_{1u} modes are infrared active, the F_{1g} , A_{2u} , 2E_u and 2F_{2u} modes are silent, and the A_{1g} , E_g and 3F_{2g} modes are Raman active.⁵¹ The A_{1g} mode represents the symmetric stretching of oxygen atoms with respect to the metal ion at the tetrahedral site, and the E_g and $\text{F}_{2g}(3)$ modes represent the symmetric and asymmetric bending of oxygen with respect to the metal ion at the octahedral site, respectively. The $\text{F}_{2g}(2)$ mode represents the asymmetric stretching of oxygen atoms with respect to the metal ion also at the octahedral site, while the $\text{F}_{2g}(1)$ mode represents the translation movement of the whole FeO_4 (Fe is at the tetrahedral site).^{50,52}

Figure 8 shows the Raman spectra of samples prepared with and without oleic acid. The peak at $\sim 177 \text{ cm}^{-1}$ represents the $\text{F}_{2g}(1)$ mode, the peaks at ~ 300 and $\sim 335 \text{ cm}^{-1}$ represent the E_g mode, the peaks at ~ 466 and $\sim 543 \text{ cm}^{-1}$ represent the $\text{F}_{2g}(2)$ and $\text{F}_{2g}(3)$ modes, respectively, while the high-frequency peaks at ~ 615 and $\sim 680 \text{ cm}^{-1}$ belong to the A_{1g} mode.^{51,52} Based on a factor-group analysis five Raman-active modes were expected. However, a deconvolution with a Lorentzian function identified the presence of seven components. The Raman spectra reported in refs 53–55 and 56 also show the presence of seven Raman-active modes at similar positions. Jacintho et al.⁵³ explained that the additional modes in the CFO can appear due to symmetry breaking. Furthermore, since the wavelength of the exciting radiation is much larger than the particle sizes, the momentum-conservation law is broken and thus extra modes are observed.^{53,57}

Figure 9a–c shows the Raman shift of three characteristic $\text{F}_{2g}(2)$ ($\sim 466 \text{ cm}^{-1}$), A_{1g} ($\sim 615 \text{ cm}^{-1}$), and A_{1g} ($\sim 680 \text{ cm}^{-1}$) Raman modes of nanosized CFO, prepared at different oleic acid concentrations. Compared to the sample prepared without oleic acid a red shift is initially observed (from 0 to 0.1 M oleic acid). A further increase of C_{OA} up to 0.25 M oleic acid, causes a blue shift, while for higher concentrations the position of all three modes remains relatively constant. There are several reports of possible reasons for the appearance of the red shift. In the case of zinc ferrite the red shift was explained by crystalline disorder, the presence of grain boundaries,⁵⁸ as well as by a decrease of the particle size.⁵⁹ In our study the decrease of the particle size from $\sim 19 \text{ nm}$ (without oleic acid) to $\sim 15 \text{ nm}$ (0.1 M oleic acid) was observed based on the XRD and TEM results (Figure 1a and Figure 2a) and thus explains the red shift. Above 0.1 M oleic acid the blue shift can be related to the lattice strain created by the oleic acid capping layer due to its covalent bonding with the surface metal ions.³² At 0.25 M the particles became saturated with oleic acid (Figure 4b) and therefore the positions of the Raman modes are not affected to any great extent. The presence of a critical concentration is clearly visible if the peak separation, i.e., the $\Delta\nu$ values, is plotted against the oleic acid concentration (Figure 9d,e). It can

be seen that the separation of the A_{1g} ($\sim 680 \text{ cm}^{-1}$) and $\text{F}_{2g}(2)$ ($\sim 466 \text{ cm}^{-1}$), as well as the A_{1g} ($\sim 680 \text{ cm}^{-1}$) and A_{1g} ($\sim 615 \text{ cm}^{-1}$) peaks reaches a minimum at 0.25 M. The intensity ratio of A_{1g} ($\sim 680 \text{ cm}^{-1}$) to A_{1g} ($\sim 615 \text{ cm}^{-1}$) modes can be used for an assessment of the cation redistribution in CFO NPs. The experimental methods that can be used for assessment of cation distribution factor, δ , range from XRD^{60–62} and neutron diffraction,⁶³ X-ray absorption near edge structure (XANES), and extended X-ray absorption fine structure (EXAFS) analysis^{64,65} to the most commonly applied Mössbauer spectroscopy.^{20,66} Although the investigation of spinel structure by Raman spectroscopy started a few decades ago,⁶⁷ only recently did Nakagomi et al.⁶⁸ show that Raman spectroscopy can reveal the degree of cation distribution between A and B sites.

In the Nakagomi et al.⁶⁸ study the cation distribution factor in $\text{Mg}_x\text{Fe}_{3-x}\text{O}_4$ nanoparticles was initially obtained by Mössbauer spectroscopy and correlated with the results of Raman spectroscopy. In the study the Mg amount in $\text{Mg}_x\text{Fe}_{3-x}\text{O}_4$ was gradually increased, which was followed by splitting of the Raman A_{1g} mode into two components. Due to the large mass difference between Fe and Mg, the mode at $\sim 670 \text{ cm}^{-1}$ was assigned to symmetric stretching of oxygen atoms with respect to the Fe^{3+} , while the mode at $\sim 715 \text{ cm}^{-1}$ was assigned to symmetric stretching of oxygen atoms with respect to the lighter Mg^{2+} ions. The cation distribution factor, δ , which reflects the Mg content in the tetrahedral A site, was obtained by using the equation:

$$\delta_{\text{Raman}}^{\text{A}}(\text{Mg}) = \frac{I_{\text{Mg}}}{2(I_{\text{Mg}} + RI_{\text{Fe}})} \quad (4)$$

where the I_{Mg} and I_{Fe} are the intensities of $\text{A}_{1g}(\text{Mg}-\text{O})$ and $\text{A}_{1g}(\text{Fe}-\text{O})$ modes, respectively. The parameter R , which totals 0.5, was obtained empirically as a value that provided satisfactory agreement between Raman and Mössbauer spectroscopy for the Mg content in the A site. Nakagomi et al.⁶⁸ described R as the relative oscillator strength of the $\text{Mg}-\text{O}_4-[(12-n)\text{Fe} + n\text{Mg}]$ bonds with respect to the $\text{Fe}-\text{O}_4-[(12-n)\text{Fe} + n\text{Mg}]$ bonds, where n is the number of bounded Mg ions. In our study the two A_{1g} modes, centered at 603–618 and 672–683 cm^{-1} , are clearly visible in all investigated cases (Figure 8). However, their assignment, following the approach of Nakagomi et al.,⁶⁸ is complicated due to similar masses of Co and Fe ions. In a rather simplistic description the vibration frequency of $\text{A}_{1g}(\text{Co}-\text{O})$ and $\text{A}_{1g}(\text{Fe}-\text{O})$ modes can be written as $\nu = (1/2\pi)(k/\mu)^{1/2}$, where μ is a reduced mass of the vibrating pair and k is a force constant (bond strength). In a recent study Kumar et al.⁶⁰ investigated the cation distribution of nanosized cobalt ferrite using the XRD method. The reported values of Co–O and Fe–O bond lengths in CFO obtained by the coprecipitation method and treatment at 200 °C, due to the similarity with our synthesis procedure, can be used to calculate the ratio of vibration frequencies $\nu_{(\text{Co}-\text{O})}/\nu_{(\text{Fe}-\text{O})}$. In this calculation, since bond strength is reciprocal to bond length,⁶⁹ by approximating to some degree, k can be written as ($k = \text{constant}/\text{bond length}$). The obtained $\nu_{(\text{Co}-\text{O})}/\nu_{(\text{Fe}-\text{O})}$ ratio of 1.04 is surprisingly similar to the ratio of the positions of the two A_{1g} modes centered at 603–618 and 672–683 cm^{-1} (average = 1.11). Such simplified analysis shows that the mode centered at 672–683 cm^{-1} can be ascribed to the $\text{A}_{1g}(\text{Co}-\text{O})$ mode, while the one centered at 603–618 cm^{-1} can be ascribed to the $\text{A}_{1g}(\text{Fe}-\text{O})$ mode.

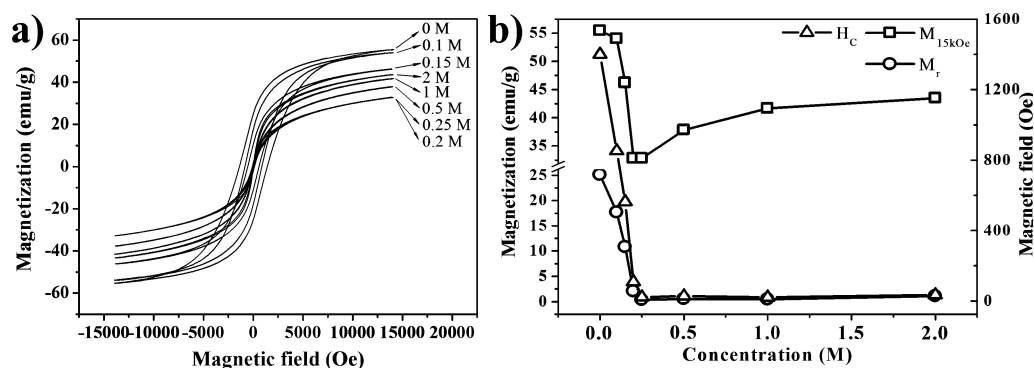


Figure 10. (a) Room temperature M vs H dependence of CFO NPs synthesized with different oleic acid concentrations. (b) Magnetization (M_{15kOe}) at 15 kOe, remanent magnetization (M_r), and coercivity (H_c) values versus oleic acid concentration.

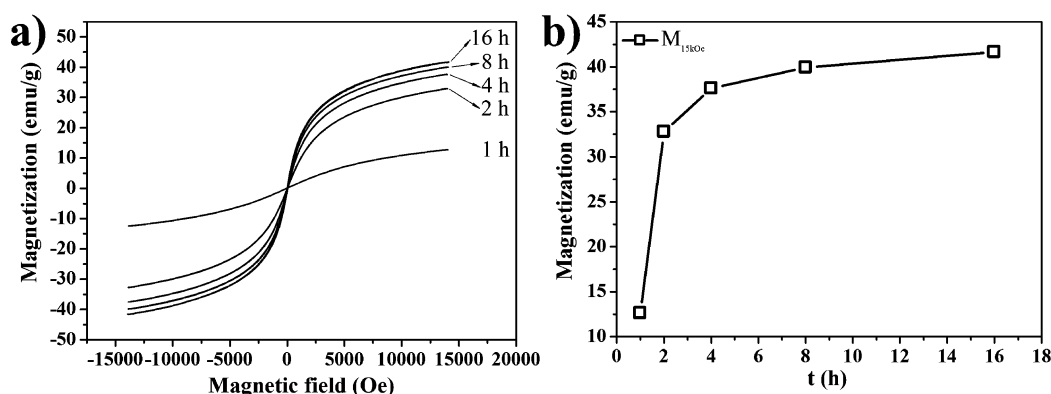


Figure 11. (a) Room temperature M vs H dependence of CFO NPs solvothermally treated for 1–16 h. (b) Magnetization at 15 kOe versus the synthesis time.

This enabled us to calculate the distribution factor using eq 4, while assuming $R = 0.5$. The content of Co ions in the tetrahedral site, δ , going from 0, 0.1, 0.15, 0.2, 0.25, 1, and 2 M oleic acid is 0.36, 0.33, 0.36, 0.33, 0.35, 0.35, and 0.34, respectively. The reported values of the cation distribution factor of Co in the tetrahedral site of bulk and nanosized CFO range from 0.20 to 0.32,^{64,65,70,71} which is in good agreement with our results. Especially encouraging is the agreement with the Repko et al.²⁰ study ($\delta = 0.33$) that was used as a starting point for our examination of the effect of oleic acid concentration. Our results clearly show that oleic acid has no influence on cation distribution factor, i.e., inversion degree (Figure 9f).

3.4. Magnetic Measurements. **3.4.1. VSM Measurements.** The first insight into magnetic properties of the CFO NPs synthesized with different concentrations of oleic acid we obtained using VSM. Figure 10a shows the room temperature measurements of magnetization as a function of magnetic field up to ± 15 kOe. One can clearly see two different types of CFO NPs behavior: the NPs prepared with oleic acid concentration below 0.2 M demonstrate long-range order even at room temperature, while the NPs prepared with oleic acid concentration above 0.25 M show superparamagnetic behavior. This dual magnetic behavior is summarized in Figure 10b where the magnetization at 15 kOe (M_{15kOe}), the remanent magnetization (M_r), and coercivity (H_c) versus oleic acid concentration are shown. The magnetic measurements agree with other characterization methods and confirm oleic acid concentration 0.25 ± 0.05 M as critical.

We also examined the room temperature magnetization versus magnetic field strength of CFO NPs that were solvothermally treated for different times (Figure 11a). The M versus H dependence confirmed the superparamagnetic behavior of the CFO NPs prepared with 1 M oleic acid concentration. Interesting, for these NPs the M_{15kOe} value increases almost three times, with the prolongation of the synthesis time (Figure 11b). Longer synthesis times ($t > 4$ h) affect the M_{15kOe} only slightly and can be related to the growth of NPs according to the TEM observations (Figure 3b–f). A similar trend was also observed in the case of the hydrothermally derived CFO NPs.⁷²

3.4.2. Low-Temperature SQUID Measurements. To examine the magnetic properties of CFO NPs in more detail we also performed the usual low-temperature magnetic measurements. The results of the temperature (2–300 K) dependence of magnetization at 100 Oe in the ZFC and FC regime are shown in Figure 12. ZFC curves are characterized with the CFO NPs concentration dependent broad maximum: the decrease of oleic acid concentration from 1 to 0.2 M during sample preparation moves the maximum to higher temperatures (188 to 228 K). The T_{max} value for CFO NPs prepared with 1 M oleic acid concentration corresponds well with the literature data.²⁰ Sample prepared with 0.15 M oleic acid concentration contains bigger NPs with a diameter of 11 nm. For this sample, we could not observe a ZFC maximum even at 300 K. As explained by Peddis et al.¹⁷ the shift of T_{max} to higher temperatures can occur due to the increase of volume anisotropy and interparticle interaction. Since the particle size of investigated samples is relatively constant the shift of T_{max} values to higher temper-

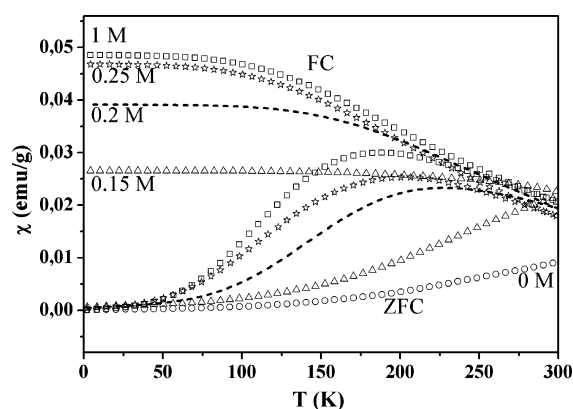


Figure 12. ZFC and FC curves of CFO NPs synthesized with different oleic acid concentrations (measured in a magnetic field of 100 Oe).

atures with a decrease of oleic acid concentration is due to increased interparticle interaction, which is already indicated by corresponding TEM images (Figure 2d,e,g). A connection of T_{\max} and blocking temperature T_b can be written in first approximation as $T_{\max} = AT_b$ with the constant A between 1 and 2.⁷³ Thus, for the investigated system the blocking temperature increases with a decrease of oleic acid concentration and relates to a gradual change of the samples' magnetic order; i.e., from superparamagnetic to long-range order regime at room temperature.

The low-temperature parts of FC curves demonstrate for samples prepared with oleic acid concentration between 1 and 0.15 M a temperature-independent part below about 80 K. This indicates that in the low-temperature region the dipolar interaction is prevailing (energy due to dipolar interaction is proportional to μ^2/d^3 in the point magnetic dipole approximation⁷⁴) and thus excludes the presence of long-range order

or paramagnetic behavior. We can see in Figure 12 very similar behavior in magnetic susceptibility (χ) vs T for samples with oleic acid concentration down to 0.25 M. Different values of χ at $H = 100$ Oe and 2 K for sample with 0.2 M oleic acid concentration can be associated with the change of nanoparticle shape and size as demonstrated by TEM results in Figure 2d. On the other hand, the sample with the oleic acid concentration of 0.15 M, consisting of a mixture of nanoplatelets and spherical NPs (Figure 2c), has at 2 K about 45% lower value of χ compared to the 1 M sample. This might be due to the fact that we could not start the FC measurement at temperatures far above the blocking temperature.

The M vs H hysteresis loops measured at 5 K for samples prepared with different oleic acid concentrations are shown in Figure 13. These measurements were performed at a temperature well below T_b . The sample with 1 M oleic acid concentration was also measured at 300 K (above T_b) and show superparamagnetic behavior, similar to one from VSM measurements. The low-temperature hysteresis loops reach the highest, almost saturated value of magnetization for the uncoated CFO NPs. The value of magnetization is about 20% higher than the corresponding value of the CFO NPs prepared with 1 M oleic acid. Simultaneously, the observed value of M_r shows about 35% reduction with respect to the M_r of uncoated CFO NPs. Comparing the M_r/M_s values for all the measured samples we noticed that M_r/M_s reaches 0.77 for the uncoated CFO NPs and values between 0.55 and 0.60 for all the coated CFO NPs. These M_r/M_s values indicate the prevailing cubic anisotropy in the uncoated CFO sample and the uniaxial anisotropy for all the coated CFO NPs samples.

Due to the bonding of oleic acid to metal cations the surface of NPs becomes coordinated because the symmetry of the surface resembles that of the core more closely.¹⁷ As a result, the spin–orbit coupling, which is responsible for magnetic anisotropy, becomes smaller. Thus, the bonding of oleic acid

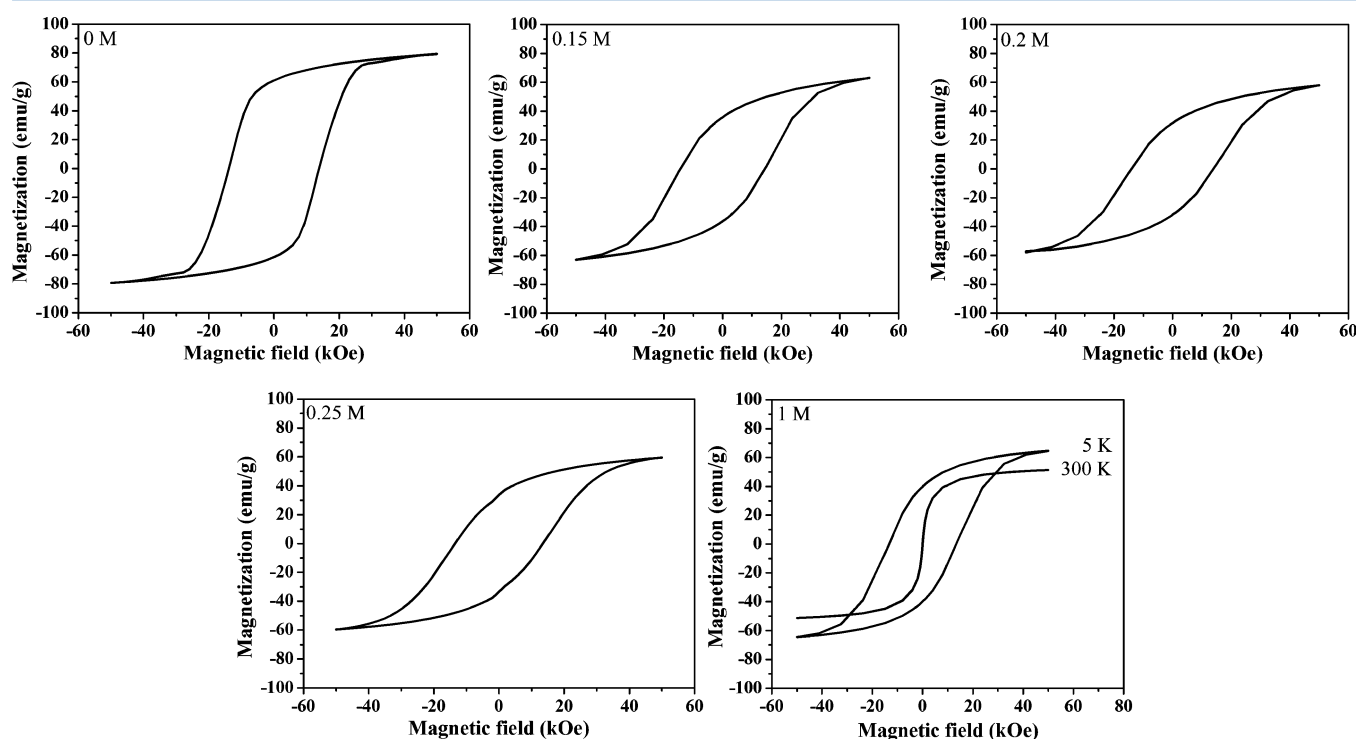


Figure 13. M vs H loops of CFO NPs synthesized with different oleic acid concentrations measured at $T = 5$ K.

decreases NPs surface anisotropy, which is further demonstrated in decreased coercivity of NPs. In the investigated system variation of the coercivity field is very small; however, at 5 K the value decreases from 14.4 kOe to 13.4 kOe as the oleic acid concentration increases from 0.15 to 1 M. Furthermore, for samples prepared with 0.25 and 1 M oleic acid the coercivity values are the same, which again indicates that critical concentration of the ligand was surpassed, leading to comparable surface properties.

4. CONCLUSION

In this work we have studied the effect of oleic acid concentration on the physicochemical properties of solvothermally derived CFO NPs. The results showed that oleic acid enables a control of the size, shape, and agglomeration of the CFO NPs. We identified 0.25 M oleic acid as a critical concentration, across which the biggest changes in properties occur. The TG and FT-IR analyses revealed that oleic acid forms covalent bidentate with metal ions on the particle surface and a complete monolayer at the critical concentration. For oleic acid concentrations up to 0.25 M a decrease of particle size from 19 to 5 nm and a morphology change from nanoplatelets to sphere-like NPs were observed, while a further increase of the oleic acid concentration has almost no effect on the corresponding properties. Raman spectroscopy suggests that the surface of the CFO NPs is under strain because of the oleic acid capping layer. It also shows that the cation distribution does not depend on the oleic acid concentration and thus it has no effect on the composition and structure of the CFO. The magnetic properties of the CFO NPs are directly related to the particle size, their interactions, and surface anisotropy, and show that control of the oleic acid concentration enables optimization of NPs magnetic behavior. The results of our study show that solvothermally derived CFO with oleic acid-controlled structural and magnetic properties can be used in a number of applications. For instance, in combination with piezoelectric materials CFO NPs can be used in the design of magnetoelectric devices with structuring on the nanoscopic level.

■ ASSOCIATED CONTENT

Supporting Information

Additional information on particle size distribution, TG and DSC curves, as well as QMS spectra of different mass-to-charge ratio of CFO NPs prepared with different oleic acid and different synthesis time. This material is available free of charge via the Internet at <http://pubs.acs.org>.

■ AUTHOR INFORMATION

Corresponding Author

*E-mail: matjaz.spreitzer@ijs.si. Tel: +386 1 477 3705. Fax: +386 1 477 3875.

Notes

The authors declare no competing financial interest.

■ ACKNOWLEDGMENTS

The research was financially supported by the Ministry of Higher Education, Science and Technology of the Republic of Slovenia (Grant No. 1000-10-310111). The authors want to express appreciation to Mojca Otoničar, Dr. Marjeta Maček-Kržmanc, Dr. Tomaž Skapin, and Dr. Zvonko Jagličić for the

TEM, TG/DSC, FT-IR, and SQUID measurements, respectively.

■ REFERENCES

- (1) Philip, J.; Rao, C. B.; Jayakumar, T.; Raj, B. A new optical technique for detection of defects in ferromagnetic materials and components. *NDT&E Int.* **2000**, *33*, 289–295.
- (2) John, P.; Jayakumar, T.; Kalyanasundaram, P.; Raj, B. A tunable optical filter. *Meas. Sci. Technol.* **2003**, *14*, 1289–1294.
- (3) Chiba, D.; Yamanouchi, M.; Matsukura, F.; Ohno, H. Electrical Manipulation of Magnetization Reversal in a Ferromagnetic Semiconductor. *Science* **2003**, *301*, 943–945.
- (4) Amulevicius, A.; Baltrunas, D.; Mazeika, K.; Fannin, P. C.; Perfiliev, Y. D. A study of the magnetic properties of mixed ferrite nanoparticles in ferrofluids. *J. Mol. Liq.* **2007**, *133*, 152–158.
- (5) Dallas, P.; Kelarakis, A.; Sahore, R.; DiSalvo, F. J.; Livi, S.; Giannelis, E. P. Self-suspended permanent magnetic FePt ferrofluids. *J. Colloid Interface Sci.* **2013**, *407*, 1–7.
- (6) Casula, M. F.; Corrias, A.; Arosio, P.; Lascialfari, A.; Sen, T.; Floris, P.; Bruce, I. J. Design of water-based ferrofluids as contrast agents for magnetic resonance imaging. *J. Colloid Interface Sci.* **2011**, *357*, 50–55.
- (7) Lin, Y.-J.; Yang, J.-Y.; Shu, T.-Y.; Lin, T.-Y.; Chen, Y.-Y.; Su, M.-Y.; Li, W.-J.; Liu, M.-Y. Detection of C-reactive protein based on magnetic nanoparticles and capillary zone electrophoresis with laser-induced fluorescence detection. *J. Chromatogr. A* **2013**, *1315*, 188–194.
- (8) Tan, P.; Lei, C.; Liu, X.; Qing, M.; Nie, Z.; Guo, M.; Huang, Y.; Yao, S. Fluorescent detection of protein kinase based on zirconium ions-immobilized magnetic nanoparticles. *Anal. Chim. Acta* **2013**, *780*, 89–94.
- (9) Wang, Y.; Zhang, X.; Liu, Y.; Lv, S.; Jiang, Y.; Zhang, Y.; Liu, H.; Liu, Y.; Yang, J. L₁₀ CoPt–Cu nanoparticles for high-density magnetic recording by sol–gel technique. *J. Alloys Compd.* **2014**, *582*, 511–514.
- (10) Mendoza-Reséndez, R.; Morales, M. P.; Serna, C. J. Reduction mechanism of uniform iron oxide nanoparticles to metal used as recording media. *Mater. Sci. Eng., C* **2003**, *23*, 1139–1142.
- (11) El-Shobaky, G. A.; Turkey, A. M.; Mostafa, N. Y.; Mohamed, S. K. Effect of preparation conditions on physicochemical, surface and catalytic properties of cobalt ferrite prepared by coprecipitation. *J. Alloys Compd.* **2010**, *493*, 415–422.
- (12) Sharifi, I.; Shokrollahi, H.; Doroodmand, M. M.; Safi, R. Magnetic and structural studies on CoFe₂O₄ nanoparticles synthesized by co-precipitation, normal micelles and reverse micelles methods. *J. Magn. Magn. Mater.* **2012**, *324*, 1854–1861.
- (13) Molazemi, M.; Shokrollahi, H.; Hashemi, B. The investigation of the compression and tension behavior of the cobalt ferrite magnetorheological fluids synthesized by co-precipitation. *J. Magn. Magn. Mater.* **2013**, *346*, 107–112.
- (14) Sanpo, N.; Berndt, C. C.; Wang, J. Microstructural and antibacterial properties of zinc-substituted cobalt ferrite nanopowders synthesized by sol-gel methods. *J. Appl. Phys.* **2012**, *112*, 084333.
- (15) Kumar, S.; Singh, V.; Aggarwal, S.; Mandal, U. K.; Kotnala, R. K. Monodisperse Co, Zn-Ferrite nanocrystals: Controlled synthesis, characterization and magnetic properties. *J. Magn. Magn. Mater.* **2012**, *324*, 3683–3689.
- (16) Vestal, C. R.; Zhang, Z. J. Magnetic spinel ferrite nanoparticles from microemulsions. *Int. J. Nanotechnol.* **2004**, *1*, 240–263.
- (17) Peddis, D.; Orrù, F.; Ardu, A.; Cannas, C.; Musinu, A.; Piccaluga, G. Interparticle Interactions and Magnetic Anisotropy in Cobalt Ferrite Nanoparticles: Influence of Molecular Coating. *Chem. Mater.* **2012**, *24*, 1062–1071.
- (18) Manova, E.; Paneva, D.; Kunev, B.; Estournès, Cl.; Rivière, E.; Tenchev, K.; Léaustic, A.; Mitov, I. Mechanochemical synthesis and characterization of nanodimensional iron-cobalt spinel oxides. *J. Alloys Compd.* **2009**, *485*, 356–361.
- (19) Singh, M.; Ulbrich, P.; Prokopec, V.; Svoboda, P.; Šantavá, E.; Štěpánek, F. Effect of hydrophobic coating on the magnetic anisotropy

and radiofrequency heating of γ -Fe₂O₃ nanoparticles. *J. Magn. Magn. Mater.* **2013**, 339, 106–113.

(20) Repko, A.; Nižňanský, D.; Poltiová-Vejpravová, J. A study of oleic acid-based hydrothermal preparation of CoFe₂O₄ nanoparticles. *J. Nanopart. Res.* **2011**, 13, S021–S031.

(21) Zhang, K.; Holloway, T.; Pradhan, A. K. Magnetic behavior of nanocrystalline CoFe₂O₄. *J. Magn. Magn. Mater.* **2011**, 323, 1616–1622.

(22) Vestal, C. R.; Zhang, Z. J. Effects of Surface Coordination Chemistry on the Magnetic Properties of MnFe₂O₄ Spinel Ferrite Nanoparticles. *J. Am. Chem. Soc.* **2003**, 125, 9828–9833.

(23) Sun, S.; Zeng, H.; Robinson, D. B.; Raoux, S.; Rice, P. M.; Wang, S. X.; Li, G. Monodisperse MFe₂O₄ (M = Fe, Co, Mn) Nanoparticles. *J. Am. Chem. Soc.* **2004**, 126, 273–279.

(24) Yoshimura, M.; Byrappa, K. Hydrothermal processing of materials: past, present and future. *J. Mater. Sci.* **2008**, 43, 2085–2103.

(25) Wu, N.; Fu, L.; Su, M.; Aslam, M.; Wong, K. C.; Dravid, V. P. Interaction of Fatty Acid Monolayers with Cobalt Nanoparticles. *Nano Lett.* **2004**, 4, 383–386.

(26) Zhang, L.; He, R.; Gu, H.-C. Oleic acid coating on the monodisperse magnetite nanoparticles. *Appl. Surf. Sci.* **2006**, 253, 2611–2617.

(27) Tadmor, R.; Rosensweig, R. E.; Frey, J.; Klein, J. Resolving the Puzzle of Ferrofluid Dispersants. *Langmuir* **2000**, 16, 9117–9120.

(28) Ayyappan, S.; Philip, J.; Raj, B. Effect of Digestion Time on Size and Magnetic Properties of Spinel CoFe₂O₄ Nanoparticles. *J. Phys. Chem. C* **2009**, 113, 590–596.

(29) Davies, K. J.; Wells, S.; Charles, S. W. The effect of temperature and oleate adsorption on the growth of maghemite particles. *J. Magn. Magn. Mater.* **1993**, 122, 24–28.

(30) Gong, T.; Yang, D.; Hu, J.; Yang, W.; Wang, C.; Lu, J. Q. Preparation of monodispersed hybrid nanospheres with high magnetite content from uniform Fe₃O₄ clusters. *Colloids Surf., A* **2009**, 339, 232–239.

(31) Lu, Y.; Lu, X.; Brian, T.; Mayers, T. H.; Xia, Y. Synthesis and characterization of magnetic Co nanoparticles: A comparison study of three different capping surfactants. *J. Solid State Chem.* **2008**, 181, 1530–1538.

(32) Limaye, M. V.; Singh, S. B.; Date, S. K.; Kothari, D.; Reddy, V. R.; Gupta, A.; Sathe, V.; Choudhary, R. J.; Kulkarni, S. K. High Coercivity of Oleic Acid Capped CoFe₂O₄ Nanoparticles at Room Temperature. *J. Phys. Chem. B* **2009**, 113, 9070–9076.

(33) Park, J.; An, K.; Hwang, Y.; Park, J.-G.; Noh, H.-J.; Kim, J.-Y.; Park, J.-H.; Hwang, N.-M.; Hyeon, T. Ultra-large-scale syntheses of monodisperse nanocrystals. *Nat. Mater.* **2004**, 3, 891–895.

(34) Redl, F. X.; Black, C. T.; Papaefthymiou, G. C.; Sandstrom, R. L.; Yin, M.; Zeng, H.; Murray, C. M.; O'Brien, S. P. Magnetic, Electronic, and Structural Characterization of Nonstoichiometric Iron Oxides at the Nanoscale. *J. Am. Chem. Soc.* **2004**, 126, 14583–14599.

(35) Ahnizay, A.; Seisenbaeva, G. A.; Häggström, L.; Kamali, S.; Kessler, V. G.; Nordblad, P.; Johansson, C.; Bergström, L. Preparation of iron oxide nanocrystals by surfactant-free or oleic acid-assisted thermal decomposition of a Fe(III) alkoxide. *J. Magn. Magn. Mater.* **2008**, 320, 781–787.

(36) Cullity, B. D. *Elements of X-Ray Diffraction*; Addison-Wesley: London, UK, 1978.

(37) Cannas, C.; Ardu, A.; Musinu, A.; Peddis, D.; Piccaluga, G. Spherical Nanoporous Assemblies of Iso-Oriented Cobalt Ferrite Nanoparticles: Synthesis, Microstructure, and Magnetic Properties. *Chem. Mater.* **2008**, 20, 6364–6371.

(38) Peddis, D.; Cannas, C.; Musinu, A.; Ardu, A.; Orrù, F.; Fioriani, D.; Laureti, S.; Rinaldi, D.; Muscas, G.; Concas, G.; Piccaluga, G. Beyond the Effect of Particle Size: Influence of CoFe₂O₄ Nanoparticle Arrangements on Magnetic Properties. *Chem. Mater.* **2013**, 25, 2005–2013.

(39) Roca, A. G.; Morales, M. P.; Grady, K. O.; Serna, C. J. Structural and magnetic properties of uniform magnetite nanoparticles prepared by high temperature decomposition of organic precursors. *Nanotechnology* **2006**, 17, 2783–2788.

(40) Farooq, H.; Ahmad, M. R.; Jamil, Y.; Hafeez, A.; Mahmood, Z.; Mahmood, T. Structural and Dielectric Properties of Manganese Ferrite Nanoparticles. *J. Basic Appl. Sci.* **2012**, 8, 597–601.

(41) Goldman, A. *Modern Ferrite Technology*; Springer: New York, NY, 2006.

(42) Ayyappan, S.; Gnanaprakash, G.; Panneerselvam, G.; Antony, M. P.; Philip, P. Effect of Surfactant Monolayer on Reduction of Fe₃O₄ Nanoparticles under Vacuum. *J. Phys. Chem. C* **2008**, 112, 18376–18383.

(43) Gnanaprakash, G.; Philip, J.; Jayakumar, T.; Raj, B. Effect of Digestion Time and Alkali Addition Rate on Physical Properties of Magnetite Nanoparticles. *J. Phys. Chem. B* **2007**, 111, 7978–7986.

(44) van Ewijk, G. A.; Vroege, G. J.; Philipse, A. P. Convenient preparation methods for magnetic colloids. *J. Magn. Magn. Mater.* **1999**, 201, 31–33.

(45) Ayyappan, S.; Panneerselvam, G.; Antony, M. P.; Philip, J. High temperature stability of surfactant capped CoFe₂O₄ nanoparticles. *Mater. Chem. Phys.* **2011**, 130, 1300–1306.

(46) Rana, S.; Philip, J.; Raj, B. Micelle based synthesis of cobalt ferrite nanoparticles and its characterization using Fourier Transform Infrared Transmission Spectrometry and Thermogravimetry. *Mater. Chem. Phys.* **2010**, 124, 264–269.

(47) De Palma, R.; Peeters, S.; Van Bael, M. J.; Van den Rul, H.; Bonroy, K.; Laureyn, W.; Mullens, J.; Borghs, G.; Maes, G. Silane Ligand Exchange to Make Hydrophobic Superparamagnetic Nanoparticles Water-Dispersible. *Chem. Mater.* **2007**, 19, 1821–1831.

(48) Smith, B. C. *Infrared spectral interpretation: a systematic approach*; CRC press: London, UK, 1999.

(49) Mohamed, R. M.; Rashad, M. M.; Haraz, F. A.; Sigmund, W. Structure and magnetic properties of nanocrystalline cobalt ferrite powders synthesized using organic acid precursor method. *J. Magn. Magn. Mater.* **2010**, 322, 2058–2064.

(50) Chandramohan, P.; Srinivasan, M. P.; Velmurugan, S.; Narasimhan, S. V. Cation distribution and particle size effect on Raman spectrum of CoFe₂O₄. *J. Solid State Chem.* **2011**, 184, 89–96.

(51) Lazarević, Z. Ž.; Jovalekić, Č.; Rečnik, A.; Ivanovski, V. N.; Milutinović, A.; Romčević, M.; Pavlović, M. B.; Cekić, B.; Romčević, N. Ž. Preparation and characterization of spinel nickel ferrite obtained by the soft mechanochemically assisted synthesis. *Mater. Res. Bull.* **2013**, 48, 404–415.

(52) Lazarević, Z. Ž.; Jovalekić, Č.; Rečnik, A.; Ivanovski, V. N.; Mitrić, M.; Romčević, M. J.; Paunović, N.; Cekić, B. Đ.; Romčević, N. Ž. Study of manganese ferrite powders prepared by a soft mechanochemical route. *J. Alloys Compd.* **2011**, 509, 9977–9985.

(53) Jacintho, G. V. M.; Brolo, A. G.; Corio, P.; Suarez, P. A. Z.; Rubim, J. C. Structural Investigation of MFe₂O₄ (M = Fe, Co) Magnetic Fluids. *J. Phys. Chem. C* **2009**, 113, 7684–7691.

(54) Soler, M. A. G.; Melo, T. F. O.; da Silva, S. W.; Lima, E. C. D.; Pimenta, A. C. M.; Garg, V. K.; Oliveira, A. C.; Morais, P. C. Structural stability study of cobalt ferrite-based nanoparticle using micro Raman spectroscopy. *J. Magn. Magn. Mater.* **2004**, 272–276, 2357–2358.

(55) Naik, S. R.; Salker, A. V. Change in the magnetocrystalline properties of rare earth doped cobalt ferrites relative to the magnetic anisotropy. *J. Mater. Chem.* **2012**, 22, 2740–2750.

(56) Naik, S. R.; Salker, A. V.; Yusuf, S. M.; Meena, S. S. Influence of Co²⁺ distribution and spin–orbit coupling on the resultant magnetic properties of spinel cobalt ferrite nanocrystals. *J. Alloys Compd.* **2013**, 566, 54–61.

(57) Pereira, C.; Pereira, A. M.; Fernandes, C.; Rocha, M.; Mendes, R.; Fernández-García, M. P.; Guedes, A.; Tavares, P. B.; Grenèche, J.-M.; Araújo, J. P.; Cristina Freire, C. Superparamagnetic MFe₂O₄ (M = Fe, Co, Mn) Nanoparticles: Tuning the Particle Size and Magnetic Properties through a Novel One-Step Coprecipitation Route. *Chem. Mater.* **2012**, 24, 1496–1504.

(58) Singh, J. P.; Srivastava, R. C.; Agrawal, H. M.; Kumar, R. Micro-Raman investigation of nanosized zinc ferrite: effect of crystallite size and fluence of irradiation. *J. Raman Spectrosc.* **2011**, 42, 1510–1517.

(59) Liu, W.; Chan, Y.; Cai, J.; Leung, C.; Mak, C.; Wong, K.; Zhang, F.; Wu, X.; Qi, X. D. Understanding the formation of ultrafine spinel

CoFe₂O₄ nanoplatelets and their magnetic properties. *J. Appl. Phys.* **2012**, *112*, 104306.

(60) Kumar, L.; Kumar, P.; Narayan, A.; Kar, M. Rietveld analysis of XRD patterns of different sizes of nanocrystalline cobalt ferrite. *Int. Nano Lett.* **2013**, *3*, 8.

(61) Patange, S. M.; Shirsath, S. E.; Jangam, G. S.; Lohar, K. S.; Jadhav, S. S.; Jadhav, K. M. Rietveld structure refinement, cation distribution and magnetic properties of Al³⁺ substituted NiFe₂O₄ nanoparticles. *J. Appl. Phys.* **2011**, *109*, 053909.

(62) Pandit, R.; Sharma, K. K.; Kaur, P.; Kotnala, R. K.; Shah, J.; Kumar, R. Effect of Al³⁺ substitution on structural, cation distribution, electrical and magnetic properties of CoFe₂O₄. *J. Phys. Chem. Solids* **2014**, *75*, 558–569.

(63) Bræstrup, F.; Hauback, B. C.; Hansen, K. K. Temperature dependence of the cation distribution in ZnFe₂O₄ measured with high temperature neutron diffraction. *J. Solid State Chem.* **2008**, *181*, 2364–2369.

(64) Carta, D.; Casula, M. F.; Falqui, A.; Loche, G.; Mountjoy, G.; Sangregorio, C.; Corrias, A. A Structural and Magnetic Investigation of the Inversion Degree in Ferrite Nanocrystals MFe₂O₄ (M = Mn, Co, Ni). *J. Phys. Chem. C* **2009**, *113*, 8606–8615.

(65) Carta, D.; Mountjoy, G.; Navarra, G.; Casula, M. F.; Loche, D.; Marras, S.; Corrias, A. X-ray Absorption Investigation of the Formation of Cobalt Ferrite Nanoparticles in an Aerogel Silica Matrix. *J. Phys. Chem. C* **2007**, *111*, 6308–6317.

(66) Siddique, M.; Butt, N. M. Effect of particle size on degree of inversion in ferrites investigated by Mössbauer spectroscopy. *Physica B* **2010**, *405*, 4211–4215.

(67) Verble, J. L. Temperature-dependent light-scattering studies of the Verwey transition and electronic disorder in magnetite. *Phys. Rev. B* **1974**, *9*, 5236–5248.

(68) Nakagomi, F.; da Silva, S. W.; Garg, V. K.; Oliveira, A. C.; Morais, P. C.; Franco, A., Jr. Influence of the Mg-content on the cation distribution in cubic Mg_xFe_{3-x}O₄ nanoparticles. *J. Solid State Chem.* **2009**, *182*, 2423–2429.

(69) Brown, I. D.; Shannon, R. D. Empirical bond-strength-bond-length curves for oxides. *Acta Crystallogr., Sect. A* **1973**, *29*, 266–282.

(70) Vaingankar, A. S.; Khasbardar, B. V.; Patil, R. N. X-ray spectroscopic study of cobalt ferrite. *J. Phys. F: Met. Phys.* **1980**, *10*, 1615–1619.

(71) Vaingankar, A. S.; Patil, S. A.; Sahasrabudhe, V. S. Degree of inversion in cobalt ferrite by EXAFS study. *Trans. Indian Inst. Met.* **1980**, *34*, 387–389.

(72) Jovanović, S.; Spreitzer, M.; Otoničar, M.; Jeon, J.-H.; Suvorov, D. pH control of magnetic properties in precipitation-hydrothermal-derived CoFe₂O₄. *J. Alloys Compd.* **2014**, *589*, 271–277.

(73) Hansen, M. F.; Mørup, S. Estimation of blocking temperatures from ZFC/FC curves. *J. Magn. Magn. Mater.* **1999**, *203*, 214–216.

(74) Mørup, S.; Hansen, M. F.; Frandsen, C. Magnetic interactions between nanoparticles. *Beilstein J. Nanotechnol.* **2010**, *1*, 182–190.